J. Fluid Mech. (2020), *vol.* 883, A17. © Cambridge University Press 2019
doi:10.1017/jfm.2019.854

Resolvent-based estimation of space–time flow statistics

Aaron Towne[1,†], Adrián Lozano-Durán[2] and Xiang Yang[3]

[1]Department of Mechanical Engineering, University of Michigan, Ann Arbor, MI 48109, USA

[2]Center for Turbulence Research, Stanford University, Stanford, CA 94305, USA

[3]Department of Mechanical and Nuclear Engineering, Penn State University, State College, PA 16802, USA

(Received 21 January 2019; revised 2 October 2019; accepted 17 October 2019)

We develop a method to estimate space–time flow statistics from a limited set of known data. While previous work has focused on modelling spatial or temporal statistics independently, space–time statistics carry fundamental information about the physics and coherent motions of the flow and provide a starting point for low-order modelling and flow control efforts. The method is derived using a statistical interpretation of resolvent analysis. The central idea of our approach is to use known data to infer the statistics of the nonlinear terms that constitute a forcing on the linearized Navier–Stokes equations, which in turn imply values for the remaining unknown flow statistics through application of the resolvent operator. Rather than making an *a priori* assumption that the flow is dominated by the leading singular mode of the resolvent operator, as in some previous approaches, our method allows the known input data to select the most relevant portions of the resolvent operator for describing the data, making it well suited for high-rank turbulent flows. We demonstrate the predictive capabilities of the method, which we call resolvent-based estimation, using two examples: the Ginzburg–Landau equation, which serves as a convenient model for a convectively unstable flow, and a turbulent channel flow at low Reynolds number.

Key words: low-dimensional models, computational methods

1. Introduction

Practical limitations in both experiments and simulations can lead to partial knowledge of flow statistics. For example, an array of probes in an experiment provides information at a limited number of spatial locations and for a single flow quantity, e.g. velocity from hot-wires or pressure from microphones. Similarly, particle image velocimetry might provide velocity data, but not thermodynamic quantities, in a limited field of view. In simulations, one may wish to know flow statistics in a region that is not adequately resolved by the computational grid, such as unresolved near-wall regions. A Reynolds averaged Navier–Stokes simulation might provide mean flow data but not temporal statistics.

† Email address for correspondence: towne@umich.edu

The ability to use available data to estimate the statistics of flow quantities that are not directly accessible would be useful in each of these situations. For example, such a method could enable recovery of full-field statistics from a discrete set of measurements, estimates of the statistics of one variable from measurement of another or estimates for a region outside of the field of measurement or computational domain.

Several methods for estimating unknown flow statistics from a limited set of known entries have recently been developed. Beneddine *et al.* (2016) proposed a method for estimating unknown power spectral densities (PSDs) using knowledge of the mean flow field and power spectra at a few locations. This is accomplished using a least-squares fit at each frequency between the known power spectra and the leading singular response mode obtained from the resolvent operator (McKeon & Sharma 2010), which is derived from the linearized Navier–Stokes equations. This strategy explicitly assumes that the spectral content at frequencies of interest is dominated by the leading resolvent mode, and the method performs well when the matching points are located in regions where this hypothesis is valid. Specifically, excellent PSD estimates were obtained for the flow over a backward-facing step (Beneddine *et al.* 2016) and an initially laminar jet (Beneddine *et al.* 2017). A similar approach was contemporaneously proposed by Gómez *et al.* (2016*a*), but their formulation performed the least-squares fit in the time domain, with a focus on obtaining a low-rank representation of time histories rather than statistics. This approach was used by the authors to estimate oscillation in a cavity flow (Gómez *et al.* 2016*a*) and aerodynamic forces on a bluff body (Gómez, Sharma & Blackburn 2016*b*).

Zare, Jovanović & Georgiou (2017) developed a method that uses arbitrary known entries in the spatial covariance tensor to estimate the remaining unknown entries. Their approach is also based on linearized flow equations and entails solving a convex optimization problem that determines a matrix controlling the structure and statistics of the associated nonlinear forcing terms. The optimization problem is subject to two constraints on the estimated covariance tensor: it must reproduce the known entries and obey a Lyapunov equation that relates the forcing and flow statistics. Solving the constrained optimization problem requires a customized algorithm (Zare *et al.* 2017; Zare *et al.* 2017). The method provides estimates of the unknown entries of the covariance tensor as well as a stochastic dynamical model for the forcing that can be used for model-based estimation and control.

The objective of the present paper is to build on these previous methods to estimate unknown two-point space–time flow statistics. Both the PSDs (one-point temporal statistics) and spatial covariances (two-point spatial statistics) are subsets of two-point space–time correlations, so our approach represents a generalization of these previous methods in the sense that it directly targets the more general two-point space–time flow statistics. This is an important step since two-point space–time statistics contain additional, fundamental information about the flow. In particular, they carry information about coherent motions within the flow, and can even be used to define the concept of a coherent structure (Towne, Schmidt & Colonius 2018). Moreover, space–time correlations can be used to obtain time-domain estimates of the flow state via convolution with a time-varying input signal (Sasaki *et al.* 2017), which enables the development of real-time modelling and flow-control strategies.

The method developed in this paper borrows ideas from each of the previously mentioned methods. Like Beneddine *et al.* (2016) and Gómez *et al.* (2016*a*), our method is built upon the resolvent formalism of McKeon & Sharma (2010). The resolvent operator is derived from the Navier–Stokes equations linearized about the turbulent mean flow and constitutes a transfer function in the frequency domain

between terms that are nonlinear and linear with respect to fluctuations to the mean. Resolvent analysis has proven to be a useful tool for understanding and modelling a wide range of flows, including wall-bounded flows (Sharma & McKeon 2013; Morra *et al.* 2019), free-shear flows (Jeun, Nichols & Jovanović 2016; Schmidt *et al.* 2018) and aerodynamic wakes (Thomareis & Papadakis 2018; Symon, Sipp & McKeon 2019; Yeh & Taira 2019). Whereas Beneddine *et al.* (2016) constructed their model using only the first singular mode of the resolvent operator (obtained via singular value decomposition), our model relaxes this *a priori* assumption and allows the known data to self-select the relevant portion of the resolvent operator. This makes the method more applicable to turbulent flows, in which the leading resolvent mode may account for only a modest fraction of the total flow energy (Schmidt *et al.* 2018), and allows us to extend the method to cross-spectra in addition to power spectra. Due to its connection with the resolvent operator, we refer to our method as resolvent-based estimation.

Our approach also follows the underlying strategy employed by Zare *et al.* (2017) of using the known data to infer the statistics of the unknown nonlinear terms that act as a forcing on the linearized equations. Both methods can be used to estimate space–time flow statistics, but the two approaches use different types of input data, which leads to substantial algorithmic differences. The method of Zare *et al.* (2017) uses arbitrary entries of the spatial covariance tensor, which are spatial (time-integrated) quantities and need not correspond to a fixed set of measurement probes. For example, the authors developed a model for a channel flow using the one-point velocity variance and covariance terms at all wall-normal positions within the channel, but without using two-point correlations. The trade-off of these benefits is the algorithmic complexity mentioned earlier. In contrast, our method requires two-point space–time statistics as input. This could be challenging in some applications, but in many cases the same data used to compute the simpler spatial statistics can be used to obtain the two-point space–time statistics as well. This is the case whenever measurements at multiple locations are obtained simultaneously, e.g. by an array of probes or by sampling numerical data, and two-point space–time statistics can always be obtained using just two concurrent measurements. A benefit of using space–time data as input is that the resulting formulation is algorithmically simple, requiring only basic linear algebra manipulations.

The objective of our method is fundamentally different from previous studies that have used resolvent analysis to obtain low-rank reconstructions of known data. For example, Moarref *et al.* (2014) solved a convex optimization problem to determine expansion coefficients for a small set of leading resolvent modes that optimally reproduced known power spectra for a turbulent channel flow. Alternatively, Jeun *et al.* (2016) used data from a large-eddy simulation of a turbulent jet to directly compute the expansion coefficients and obtained a low-rank reconstruction of the power spectra in the acoustic field by retaining a limited number of terms in the expansion. Similarly, Morra *et al.* (2019) obtained a low-rank reconstruction of cross-spectral densities in a turbulent channel flow by computing the necessary expansion coefficients from direct numerical simulation data. Rather than reconstructing known statistics, our objective is to use limited known data to estimate unknown flow statistics.

The objective and capabilities of our method are also fundamentally different from those of the classical method of linear stochastic estimation (Adrian 1994; Bonnet *et al.* 1994) and related approaches that have recently been investigated (e.g. Encinar, Lozano-Durán & Jiménez 2018). In these methods, cross-correlations between input quantities (the measurements) and output quantities of interest (unknown flow

quantities) must be known *a priori* and are used to estimate instantaneous values or conditional averages for the quantities of interest. In contrast, our method assumes no knowledge of the output statistics (or its cross-correlation with input quantities), and instead uses input data (along with mean flow data) to estimate space–time statistics of the output quantities of interest. Accordingly, our method could in fact be used to obtain an estimate of the statistics required to perform linear stochastic estimation.

The remainder of this paper is organized as follows. The method is derived and described in § 2 and demonstrated in § 3 using two examples: a simple model problem given by the Ginzburg–Landau equation and a turbulent channel flow. Finally, § 4 summarizes the paper and discusses further improvements and applications of the method.

2. Method

Our method for estimating space–time flow statistics from limited measurements is developed in this section. After precisely defining the objective, we develop our approach to the problem and provide some alternative interpretations of the method, which help to elucidate its properties.

2.1. *Objective*

Consider a state vector of flow variables $\boldsymbol{q}(\boldsymbol{x}, t)$ that describe a flow, e.g. velocities and thermodynamic variables. The independent variables $\boldsymbol{x}$ and t represent the spatial dimensions of the problem and time, respectively. Now suppose that the two-point space–time statistics are known for a reduced set of variables

$$\boldsymbol{y} = \mathcal{C}\boldsymbol{q}, \tag{2.1}$$

where the linear operator $\mathcal{C}(\boldsymbol{x})$ selects any desired subset or linear combination of $\boldsymbol{q}$. The problem objective can now be precisely stated in terms of two-point space–time correlation tensors,

$$\text{given} \quad \boldsymbol{C}_{yy}(\boldsymbol{x}, \boldsymbol{x}', \tau) = E\{\boldsymbol{y}(\boldsymbol{x}, t)\boldsymbol{y}^*(\boldsymbol{x}', t+\tau)\}, \tag{2.2a}$$

$$\text{estimate} \quad \boldsymbol{C}_{qq}(\boldsymbol{x}, \boldsymbol{x}', \tau) = E\{\boldsymbol{q}(\boldsymbol{x}, t)\boldsymbol{q}^*(\boldsymbol{x}', t+\tau)\}. \tag{2.2b}$$

Here, $E\{\cdot\}$ is the expectation operator over time and the asterisk superscript indicates a Hermitian transpose. By defining the correlation tensors in this manner, we have restricted our attention to statistically stationary flows.

Using the relationship between space–time correlation tensors and the cross-spectral density (CSD) tensors

$$\boldsymbol{S}(\boldsymbol{x}, \boldsymbol{x}', \omega) = \int_{-\infty}^{\infty} \boldsymbol{C}(\boldsymbol{x}, \boldsymbol{x}', \tau)\mathrm{e}^{-\mathrm{i}\omega\tau}\,\mathrm{d}\tau, \tag{2.3}$$

this objective can be equivalently stated in the frequency domain for statistically stationary flows,

$$\text{given} \quad \boldsymbol{S}_{yy}(\boldsymbol{x}, \boldsymbol{x}', \omega) = E\{\hat{\boldsymbol{y}}(\boldsymbol{x}, \omega)\hat{\boldsymbol{y}}^*(\boldsymbol{x}', \omega)\}, \tag{2.4a}$$

$$\text{estimate} \quad \boldsymbol{S}_{qq}(\boldsymbol{x}, \boldsymbol{x}', \omega) = E\{\hat{\boldsymbol{q}}(\boldsymbol{x}, \omega)\hat{\boldsymbol{q}}^*(\boldsymbol{x}', \omega)\}, \tag{2.4b}$$

where $\hat{\boldsymbol{y}}(\boldsymbol{x}, \omega)$ and $\hat{\boldsymbol{q}}(\boldsymbol{x}, \omega)$ are the temporal Fourier transforms of $\boldsymbol{y}$ and $\boldsymbol{q}$, respectively, and the expectation is now taken over realizations of the flow (Bendat & Piersol 1990).

2.2. *Approach*

Our approach to this problem relies on the resolvent operator obtained from the linearized flow equations and its connection with the remaining nonlinear terms (McKeon & Sharma 2010). Accordingly, we call our method resolvent-based estimation. Begin with nonlinear flow equations of the form

$$\mathcal{G}\frac{\partial \boldsymbol{q}}{\partial t} = \boldsymbol{\mathcal{F}}(\boldsymbol{q}), \tag{2.5}$$

where $\mathcal{G}$ and $\boldsymbol{\mathcal{F}}$ are linear and nonlinear operators, respectively. Both compressible and incompressible Navier–Stokes equations can be cast in this form, and $\mathcal{G}$ is singular in the incompressible case to account for the algebraic divergence-free condition. Alternatively, the incompressible equations can be written with a non-singular $\mathcal{G}$ by projecting into a divergence-free basis to eliminate the continuity equation (Meseguer & Trefethen 2003). Additional transport equations can also be included.

Applying the Reynolds decomposition

$$\boldsymbol{q}(\boldsymbol{x}, t) = \bar{\boldsymbol{q}}(\boldsymbol{x}) + \boldsymbol{q}'(\boldsymbol{x}, t), \tag{2.6}$$

where $\bar{\boldsymbol{q}}(\boldsymbol{x})$ is the mean (time-averaged) flow, to (2.5) and isolating the terms that are linear in $\boldsymbol{q}'$ yields an equation of the form

$$\mathcal{G}\frac{\partial \boldsymbol{q}'}{\partial t} - \mathcal{A}(\bar{\boldsymbol{q}})\boldsymbol{q}' = \boldsymbol{f}(\bar{\boldsymbol{q}}, \boldsymbol{q}'), \tag{2.7}$$

where

$$\mathcal{A}(\bar{\boldsymbol{q}}) = \frac{\partial \boldsymbol{\mathcal{F}}}{\partial \boldsymbol{q}}(\bar{\boldsymbol{q}}) \tag{2.8}$$

is the linearized Navier–Stokes operator and $\boldsymbol{f}$ contains the remaining nonlinear terms. Similarly, equation (2.1) becomes

$$\boldsymbol{y}' = \mathcal{C}\boldsymbol{q}'. \tag{2.9}$$

In the frequency domain, equations (2.7) and (2.9) can be manipulated to give

$$\hat{\boldsymbol{y}} = \mathcal{R}_y \hat{\boldsymbol{f}}, \tag{2.10a}$$

$$\hat{\boldsymbol{q}} = \mathcal{R}_q \hat{\boldsymbol{f}}, \tag{2.10b}$$

where

$$\mathcal{R}_y(\boldsymbol{x}, \omega) = \mathcal{C}(\mathrm{i}\omega\mathcal{G} - \mathcal{A})^{-1}, \tag{2.11a}$$

$$\mathcal{R}_q(\boldsymbol{x}, \omega) = (\mathrm{i}\omega\mathcal{G} - \mathcal{A})^{-1} \tag{2.11b}$$

are resolvent operators associated with $\hat{\boldsymbol{y}}$ and $\hat{\boldsymbol{q}}$, respectively. Strictly speaking, only $\mathcal{R}_q$ is a formal resolvent operator, but for simplicity we will use this terminology for both operators in (2.11). We note that $\mathcal{R}_y$ bears resemblance to the component-wise input–output operators studied by Jovanović & Bamieh (2005) and Schmid (2007), except that here we use $\mathcal{C}$ to select a sparse set of measurements rather than individual, but globally defined, components of the velocity vector.

Using (2.4) and (2.10), the CSD tensors can be written in terms of these resolvent operators as

$$\boldsymbol{S}_{yy} = \mathcal{R}_y \boldsymbol{S}_{ff} \mathcal{R}_y^*, \tag{2.12a}$$

$$\boldsymbol{S}_{qq} = \mathcal{R}_q \boldsymbol{S}_{ff} \mathcal{R}_q^*, \tag{2.12b}$$

where $\boldsymbol{S}_{ff}(\boldsymbol{x}, \boldsymbol{x}', \omega) = E\{\hat{\boldsymbol{f}}(\boldsymbol{x}, \omega)\hat{\boldsymbol{f}}^*(\boldsymbol{x}', \omega)\}$ is the CSD tensor of the nonlinear term $\boldsymbol{f}$ (Semeraro *et al.* 2016; Towne, Brès & Lele 2016; Towne *et al.* 2018). We emphasize that no approximation has been made to this point; equation (2.12) is an exact expression of the Navier–Stokes equations for statistically stationary flows.

To obtain an approximation of the desired statistics $\boldsymbol{S}_{qq}$, we use the known statistics $\boldsymbol{S}_{yy}$ to estimate $\boldsymbol{S}_{ff}$. The salient question then becomes: how much can we learn about $\boldsymbol{S}_{ff}$ from $\boldsymbol{S}_{yy}$? An answer is provided by examining the singular value decomposition (SVD)

$$\mathcal{R}_y = \boldsymbol{U}_y \boldsymbol{\Sigma}_y \boldsymbol{V}_y^* \tag{2.13a}$$

$$= \boldsymbol{U}_y \begin{bmatrix} \boldsymbol{\Sigma}_1 & \boldsymbol{0} \end{bmatrix} [\boldsymbol{V}_1 \ \boldsymbol{V}_2]^*. \tag{2.13b}$$

The columns of the matrices $\boldsymbol{V}_y$ and $\boldsymbol{U}_y$ correspond to input and output modes that form orthonormal bases for $\hat{\boldsymbol{f}}$ and $\hat{\boldsymbol{y}}$, respectively. The rectangular matrix $\boldsymbol{\Sigma}_y$ contains the singular values, which determine the gain of each of the input modes to the output. Since the rank of $\mathcal{R}_y$, and thus the number of non-zero singular values, can be no greater than the number of entries in $\boldsymbol{y}$, i.e. the number of measurements, many of the input modes have no impact on the output. Accordingly, the SVD can be written in the form of (2.13*b*), where the diagonal $\boldsymbol{\Sigma}_1$ contains the non-zero singular values and the blocks $\boldsymbol{V}_1$ and $\boldsymbol{V}_2$ contain input modes that have non-zero and zero gain, respectively. It is important to note that these resolvent modes are different from those usually studied, which are given by the SVD of $\mathcal{R}_q$ (e.g. McKeon & Sharma 2010; Schmidt *et al.* 2018).

The distinction between input modes that do or do not impact the output can be used to isolate the part of $\boldsymbol{S}_{ff}$ that can be educed from knowledge of $\boldsymbol{S}_{yy}$. Since $\boldsymbol{V}_y$ provides a complete basis for $\hat{\boldsymbol{f}}$, $\boldsymbol{S}_{ff}$ can be expanded as

$$\boldsymbol{S}_{ff} = [\boldsymbol{V}_1 \ \boldsymbol{V}_2] \begin{bmatrix} \boldsymbol{F}_{11} & \boldsymbol{F}_{12} \\ \boldsymbol{F}_{21} & \boldsymbol{F}_{22} \end{bmatrix} [\boldsymbol{V}_1 \ \boldsymbol{V}_2]^*, \tag{2.14}$$

where the matrices $\boldsymbol{F}_{ij}$ represent correlations between expansion coefficients associated with each input mode (see Towne *et al.* 2018). Inserting this expansion into (2.12*a*) and using (2.13*b*) to simplify the expression gives rise to the equation

$$\boldsymbol{S}_{yy} = \boldsymbol{U}_y \boldsymbol{\Sigma}_1 \boldsymbol{F}_{11} \boldsymbol{\Sigma}_1 \boldsymbol{U}_y^*. \tag{2.15}$$

This means that only the part of $\boldsymbol{S}_{ff}$ associated with $\boldsymbol{F}_{11}$ impacts the observed statistics $\boldsymbol{S}_{yy}$; the remaining $\boldsymbol{F}_{ij}$ terms have no impact and are thus unobservable from these known data. Consequently, $\boldsymbol{F}_{11}$ contains all of the information about $\boldsymbol{S}_{ff}$ that can be inferred from $\boldsymbol{S}_{yy}$. Using the orthonormality of $\boldsymbol{U}_y$, equation (2.15) gives

$$\boldsymbol{F}_{11} = \boldsymbol{\Sigma}_1^{-1} \boldsymbol{U}_y^* \boldsymbol{S}_{yy} \boldsymbol{U}_y \boldsymbol{\Sigma}_1^{-1}. \tag{2.16}$$

The remaining terms $\boldsymbol{F}_{22}$ and $\boldsymbol{F}_{12} = \boldsymbol{F}_{21}^*$ (this equality is required to make $\boldsymbol{S}_{ff}$ Hermitian) can be arbitrarily chosen without impacting $\boldsymbol{S}_{yy}$, but these terms will impact $\boldsymbol{S}_{qq}$ and therefore must be modelled. The simplest choice, and the one used in the remainder of this paper, is to set these unknown terms to zero, leading to the approximation

$$\boldsymbol{S}_{ff} \approx \tilde{\boldsymbol{S}}_{ff} = [\boldsymbol{V}_1 \;\; \boldsymbol{V}_2] \begin{bmatrix} \boldsymbol{F}_{11} & \boldsymbol{0} \\ \boldsymbol{0} & \boldsymbol{0} \end{bmatrix} [\boldsymbol{V}_1 \;\; \boldsymbol{V}_2]^* = \boldsymbol{V}_1 \boldsymbol{F}_{11} \boldsymbol{V}_1^*. \tag{2.17}$$

We show in appendix A that this choice is identical to taking the least-squares approximation of $\boldsymbol{S}_{ff}$, which can be obtained by applying the pseudo-inverse of $\mathcal{R}_y$ and its complex conjugate to the left and right sides of (2.12*a*), respectively. That is,

$$\tilde{\boldsymbol{S}}_{ff} = \mathcal{R}_y^+ \boldsymbol{S}_{yy} (\mathcal{R}_y^+)^*, \tag{2.18}$$

where the plus superscript indicates the pseudo-inverse. Therefore, this approximation corresponds to choosing the smallest forcing (in an appropriate norm) that reproduces the known flow statistics. In what follows, a tilde accent indicates an estimated quantity.

Inserting (2.17) or (2.18) into (2.12*b*) gives the corresponding approximation of the desired flow statistics

$$\boldsymbol{S}_{qq} \approx \tilde{\boldsymbol{S}}_{qq} = \mathcal{R}_q \boldsymbol{V}_1 \boldsymbol{F}_{11} \boldsymbol{V}_1^* \mathcal{R}_q^* = \mathcal{R}_q \mathcal{R}_y^+ \boldsymbol{S}_{yy} (\mathcal{R}_y^+)^* \mathcal{R}_q^*. \tag{2.19}$$

By construction, the known statistics used as input are exactly recovered, ensuring that the approximation converges in the limit of full knowledge of the flow statistics. Other approximations can be obtained by choosing the unknown $\boldsymbol{F}_{ij}$ terms differently; a few possibilities are discussed in § 4. The estimated space–time correlation tensor can be recovered from the estimated CSD via the inverse Fourier transform

$$\boldsymbol{C}(\boldsymbol{x}, \boldsymbol{x}', \tau) = \frac{1}{2\pi} \int_{-\infty}^{\infty} \boldsymbol{S}(\boldsymbol{x}, \boldsymbol{x}', \omega) \mathrm{e}^{\mathrm{i}\omega\tau} \mathrm{d}\omega. \tag{2.20}$$

The method can also be understood in terms of a resolvent-mode expansion of $\boldsymbol{S}_{qq}$. The standard resolvent modes associated with the linearized flow equations are defined by the SVD $\mathcal{R}_q = \boldsymbol{U}_q \boldsymbol{\Sigma}_q \boldsymbol{V}_q^*$. Equation (2.19) can then be written as

$$\tilde{\boldsymbol{S}}_{qq} = \boldsymbol{U}_q \boldsymbol{\Sigma}_q \boldsymbol{S}_{\beta\beta} \boldsymbol{\Sigma}_q \boldsymbol{U}_q^*, \tag{2.21}$$

where

$$\boldsymbol{S}_{\beta\beta} = \boldsymbol{V}_q^* \boldsymbol{V}_1 \boldsymbol{F}_{11} \boldsymbol{V}_1^* \boldsymbol{V}_q \tag{2.22}$$

is the CSD of the expansion coefficients in a resolvent-mode expansion of $\hat{\boldsymbol{q}}$ (Towne *et al.* 2018). In general, $\boldsymbol{S}_{\beta\beta}$ can project onto any of the resolvent output modes in $\boldsymbol{U}_q$. Thus, the known statistics $\boldsymbol{S}_{yy}$, through their influence on $\boldsymbol{F}_{11}$, determine which resolvent modes participate in the estimate of $\boldsymbol{S}_{qq}$. This can be contrasted with the rank-1 model described earlier, in which only the leading resolvent mode is allowed to contribute. Similarly, the multi-mode extension of the rank-1 method proposed (but not implemented) by Beneddine *et al.* (2017) requires *a priori* selection of a limited number of modes of $\mathcal{R}_q$. Also note that since our method does not require the SVD of $\mathcal{R}_q$, but only of the low-rank matrix $\mathcal{R}_y$, our method is less computationally expensive than a typical resolvent analysis.

3. Examples

In this section, our method is demonstrated and analysed using two example problems: the complex Ginzburg–Landau equation and a turbulent channel flow.

3.1. *Ginzburg–Landau equation*

The Ginzburg–Landau equation has been used by several previous authors (e.g. Hunt & Crighton 1991; Bagheri *et al.* 2009; Chen & Rowley 2011; Towne *et al.* 2018) as a convenient one-dimensional model that mimics key properties of the linearized Navier–Stokes operator for real flows, such as a turbulent jet (Schmidt *et al.* 2018). The linearized equations can be written in the form of (2.7) with $\mathcal{G}$ equal to the identity matrix and

$$\mathcal{A} = -\nu\frac{\partial}{\partial x} + \gamma\frac{\partial^2}{\partial x^2} + \mu(x). \tag{3.1}$$

Several variants of the function $\mu(x)$ have been used in the literature; here the quadratic form

$$\mu(x) = (\mu_0 - c_u^2) + \frac{\mu_2}{2}x^2 \tag{3.2}$$

is adopted (Hunt & Crighton 1991; Bagheri *et al.* 2009; Chen & Rowley 2011). The parameters in (3.1) and (3.2) are set to similar values as those used by Bagheri *et al.* (2009) and Towne *et al.* (2018): $\nu = 2 + 0.2i$, $\gamma = 1 - i$, $\mu_0 = 0.3$, $c_u = 0.2$, $\mu_2 = -0.01$. Following Bagheri *et al.* (2009), the equations are discretized with a pseudo-spectral approach using $N = 220$ Hermite polynomials.

The discretized equations are stochastically excited in the time domain using forcing terms with prescribed statistics identical to those used by (Towne *et al.* 2018). In particular, the forcing is generated by convolving band-limited white noise with a kernel of the form

$$g(x, x') = \frac{1}{\sqrt{2\pi}\sigma_f}\exp\left[-\frac{1}{2}\left(\frac{x - x'}{\sigma_f}\right)^2\right]\exp\left[\mathrm{i}2\pi\frac{x - x'}{\lambda_f}\right], \tag{3.3}$$

where σ_f is the standard deviation of the envelope and λ_f is the wavelength of the filter. This leads to a forcing that is white-in-time up to the cutoff frequency but that has non-zero spatial correlation in the form of (3.3) but with σ_f replaced with $\sqrt{2}\sigma_f$. This form of the forcing statistics is qualitatively similar to those of the nonlinear forcing terms in real flows, such as a turbulent jet (Towne, Brès & Lele 2017). We use $\sigma_f = 4$ and $\lambda_f = 20$.

Although these forcing statistics are prescribed in this model problem and therefore known, this knowledge is not made available to the estimation procedure. The equations are integrated using a fourth-order embedded Runge–Kutta method (Shampine & Reichelt 1997), and a total of 10 000 snapshots of the solution are collected with spacing $\Delta t = 0.5$, leading to a Nyquist frequency of $\omega_{Nyquist} = 2\pi$. The CSD of the solution is computed from these data using Welch's (1967) method.

For the majority of the following analysis, $\boldsymbol{y}$ is defined to correspond to data obtained from three probes located at $x = -10$, 0 and 10. Other choices are considered in § 3.1.4.

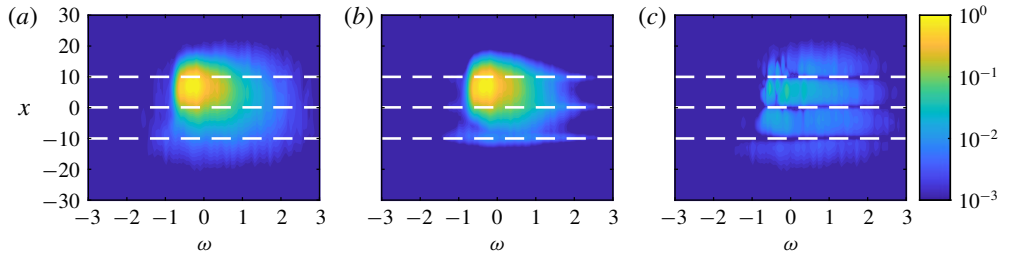

FIGURE 1. Power spectral density (PSD) as a function of ω and x for the Ginzburg–Landau model problem: (*a*) true PSD; (*b*) estimated PSD using three probes at the locations of the dashed lines; (*c*) difference between the true and estimated PSD.

3.1.1. *Power spectra*

The PSD is contained in the diagonal entries of $\boldsymbol{S}_{\boldsymbol{qq}}$, i.e. $\boldsymbol{E}_{\boldsymbol{qq}}(x, \omega) = \boldsymbol{S}_{\boldsymbol{qq}}(x, x, \omega)$. The true power spectral density for the Ginzburg–Landau model problem is shown as a function of ω and x in figure 1(*a*). A single peak is observed at $\omega \approx -0.2$ and $x \approx 5$, and the amplitude remains above 1 % of the peak over a range of about $-0.75 < \omega < 1$ and $-5 < x < 15$. The dashed lines show the x locations where the data are taken as known, and the estimation procedure will attempt to reconstruct the PSD elsewhere.

The approximation of the PSD obtained using these three probes is shown in figure 1(*b*), and the difference between the true and estimated PSD in shown in figure 1(*c*). By construction, the approximation is exact at the probe locations. The peak is well captured and the agreement is good in high-energy regions. In the lower-energy regions, the PSD is under-predicted away from the probe locations. This is a consequence of neglecting the undetermined portions of the forcing. It is likely that additional improvements could be obtained by modelling these undetermined portions of the forcing, as discussed in § 4. The total error of the PSD estimate, defined as

$$\frac{\iint |\tilde{\boldsymbol{E}}_{\boldsymbol{qq}}(x, \omega) - \boldsymbol{E}_{\boldsymbol{qq}}(x, \omega)| \, \mathrm{d}\omega \, \mathrm{d}x}{\iint \boldsymbol{E}_{\boldsymbol{qq}}(x, \omega) \, \mathrm{d}\omega \, \mathrm{d}x}, \tag{3.4}$$

is 4.9 %.

3.1.2. *Cross-spectra*

The CSD estimates are evaluated next. Figure 2 compares the real part of the true and modelled CSD at eight frequencies, which are listed in the caption. The contour levels are the same for the true and estimated data at each frequency and range from −0.5 to 1 relative to the maximum value of the true CSD. The circles indicate the locations where the CSD is known and the remaining values are to be estimated. The first six frequencies (panels *a–l*) fall within the high-energy region observed in figure 1. In these cases, the estimates accurately track the amplitudes, length scales and overall shape of the CSD as a function of frequency. The final two frequencies (panels *m–p*) fall in low-energy regions. The basic trends in the length scales and shape are still captured, but clear errors can be observed.

Figure 3 provides a more quantitative assessment of the CSD estimates. Here, the CSD relative to the reference point $x' = 0$ is plotted as a function of x for the same

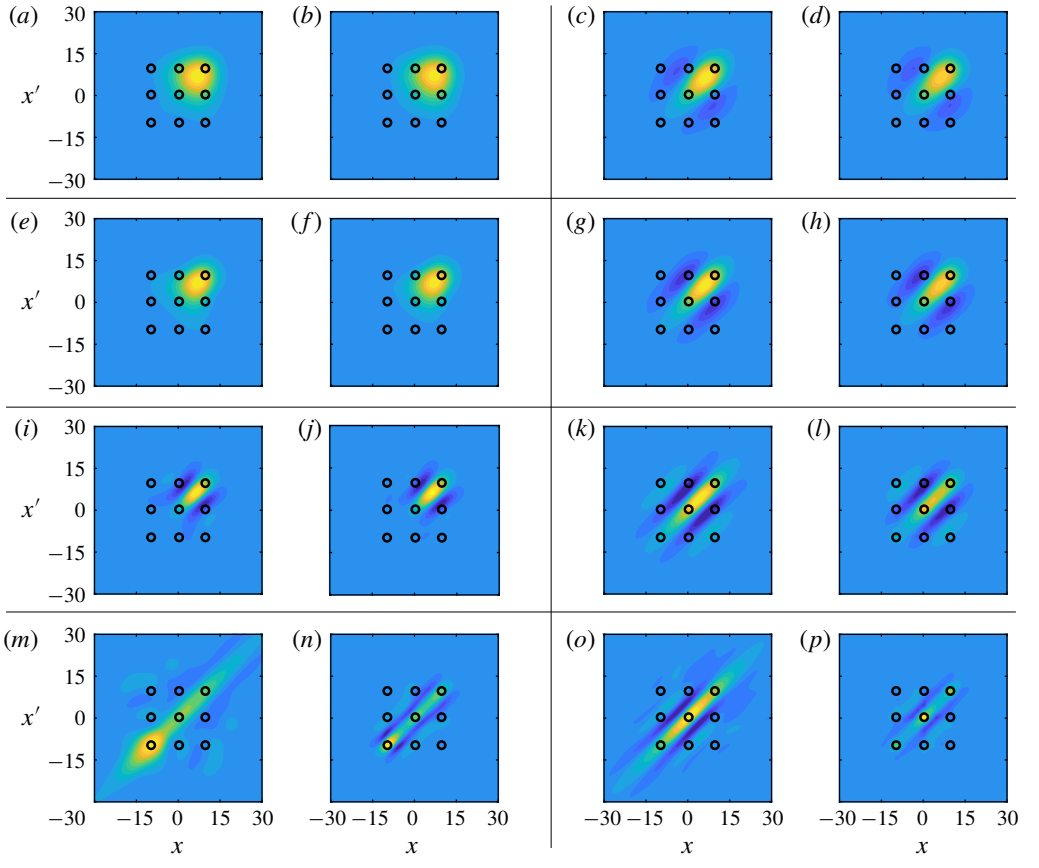

FIGURE 2. Cross-spectral density (CSD) for the frequencies (*a,b*) $\omega = 0$; (*e,f*) $\omega = -0.2$; (*i,j*) $\omega = -0.6$; (*m,n*) $\omega = -1$; (*c,d*) $\omega = 0.4$; (*g,h*) $\omega = 0.6$; (*k,l*) $\omega = 1$; (*o,p*) $\omega = 2$. In each case, the left-hand plot shows the true CSD and the right-hand plot shows the estimated values using three probes, which lead to known CSD values at the locations indicated by the small circles. The contour levels are the same for the true and estimated data at each frequency and range from the minimum to maximum values of the true CSD.

eight frequencies shown in figure 2. Both the true CSD (solid lines) and estimated CSD (dashed lines) are normalized by the maximum magnitude of the true CSD for each frequency. These plots show that the CSD estimates are quantitatively accurate for the six frequencies in the high-energy region.

3.1.3. *Space–time correlations*

The space–time correlation tensor $\boldsymbol{C_{qq}}$ can be recovered from the cross-spectral density $\boldsymbol{S_{qq}}$ using the inverse Fourier transform of (2.3). As an example, figure 4 shows the true (solid lines) and estimated (dashed lines) correlations as a function of time lag τ for three spatial locations, $x = -5$, 0 and 5. These locations correspond to a low-energy region, a probe position and the energy peak, respectively. Each curve has been scaled by the maximum value of the corresponding true correlation.

The one-point autocorrelation for each point is shown in figure 4(*a–c*). The amplitude of the autocorrelation for the low-energy point at $x = -5$ (panel *a*) is

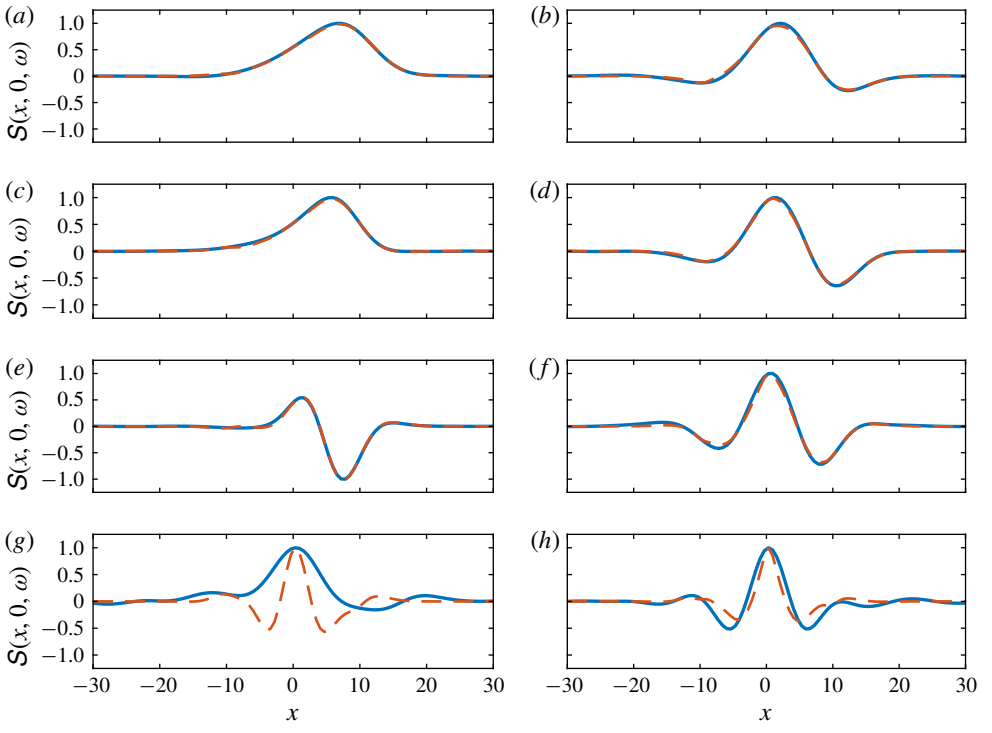

FIGURE 3. Cross-spectral density (CSD) relative to the reference point $x' = 0$ for the frequencies (*a*) $\omega = 0$; (*c*) $\omega = -0.2$; (*e*) $\omega = -0.6$; (*g*) $\omega = -1$; (*b*) $\omega = 0.4$; (*d*) $\omega = 0.6$; (*f*) $\omega = 1$; (*h*) $\omega = 2$. The solid lines show the true values, and the dashed lines show the estimates values using three probes at $x = -10$, 0 and 10.

significantly under-predicted, but the correlation length scale is well captured. The estimated autocorrelation at $x = 0$ (panel *b*) is exact since this point corresponds to one of the probe locations. The autocorrelation at $x = 5$ (panel *c*) is accurately estimated apart from a small under-prediction of the peak, which corresponds to an under-prediction of the variance.

The cross-correlations between these three points are shown in figure 4(*d–f*). The estimates are quite good in all cases, including those involving the low-energy point (panels *d* and *f*) and two unknown points (panel *f*). It is interesting that the cross-correlations involving the low-energy point are more accurate than the autocorrelation at this point. The agreement for the cross-correlation between the known and high-energy points (panel *e*) is almost perfect.

The spatial distribution of the true and estimated cross-correlation tensors at fixed values of the time lag τ is shown in figure 5. The plotted time-lag values range from $\tau = 0$ to 10; negative values need not be considered due to the symmetry

$$\boldsymbol{C}_{\boldsymbol{qq}}(\boldsymbol{x}_1, \boldsymbol{x}_2, -\tau) = \boldsymbol{C}^*_{\boldsymbol{qq}}(\boldsymbol{x}_2, \boldsymbol{x}_1, \tau). \tag{3.5}$$

The contour levels are the same in each panel and range from zero to the maximum values of the true correlation at $\tau = 0$. Again, the circles indicate the locations where the correlations are known, and the remaining values are to be estimated.

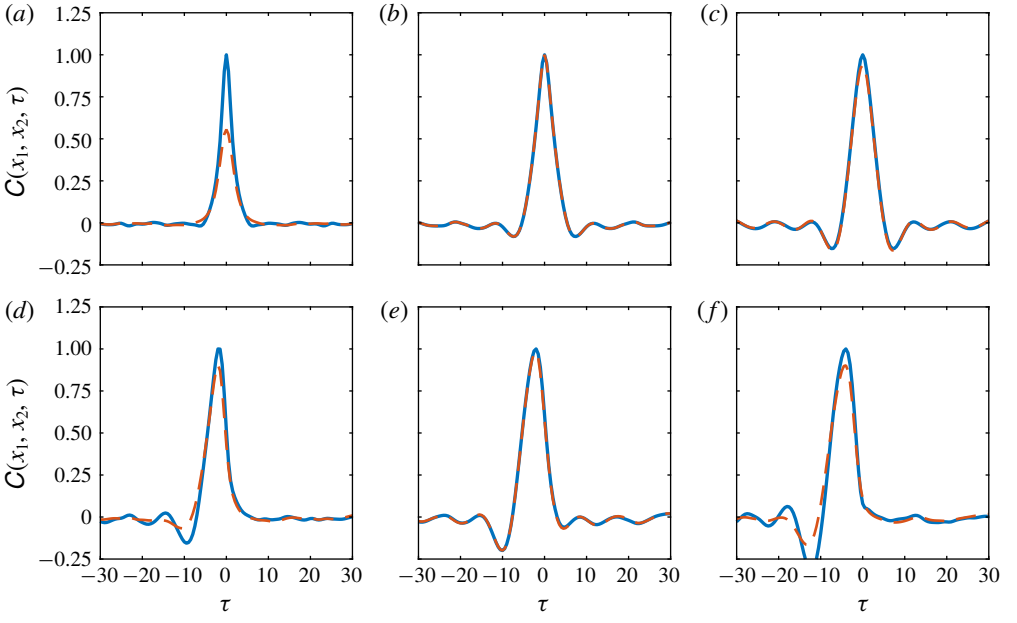

FIGURE 4. Cross-correlation as a function of time lag τ for (*a*) $x_1 = x_2 = -5$; (*b*) $x_1 = x_2 = 0$; (*c*) $x_1 = x_2 = 5$; (*d*) $x_1 = -5$, $x_2 = 0$; (*e*) $x_1 = 0$, $x_2 = 5$; (*d*) $x_1 = -5$, $x_2 = 5$. The solid lines show the true values, and the dashed lines show the estimates values using three probes at $x = -10, 0$ and 10. Both the true and estimated curves in each plot have been scaled by the maximum value of the true correlation.

The spatial correlation tensor is obtained for $\tau = 0$ and is shown in figure 5(*a*). As already observed in figure 4, the amplitudes of the correlations at zero time lag are slightly under predicted, but the spatial shape and overall amplitude are well captured. As the time lag τ is increased, the estimates faithfully track the changing amplitude and shape of the true correlations up to at least $\tau = 10$, by which point the amplitudes of the correlations are small.

3.1.4. *Impact of probe location and comparisons with the rank-1 model*

In this section, comparisons are made between the new resolvent-based estimation method described in this paper and the rank-1 method of Beneddine *et al.* (2016) that was discussed in § 1. Particular attention is given to the impact of the probe location(s) on the accuracy of the estimates provided by these two methods.

We focus on the PSD, which is the target quantity of the rank-1 model. Figure 6 compares the true PSD (*a–c*) to the estimates from the rank-1 method (*d–f*) and the new model (*g–i*) for three different sets of probe locations (columns). The integrated error metric from (3.4) is also reported in the figure for each estimate.

First, a single probe is placed at $x = 0$. In this case, the two methods provide similar estimates. Adding an additional probe in the low-energy region at $x = -10$ (second column) increases the error of the rank-1 method. This is an undesirable property; it means that poorly placed probes (where the rank-1 assumption is invalid) can obscure the information provided by well-placed probes (where the assumption is valid). More generally, this is a manifestation of the fact that the rank-1 method does not necessarily converge with increasing input information (Towne *et al.* 2018).

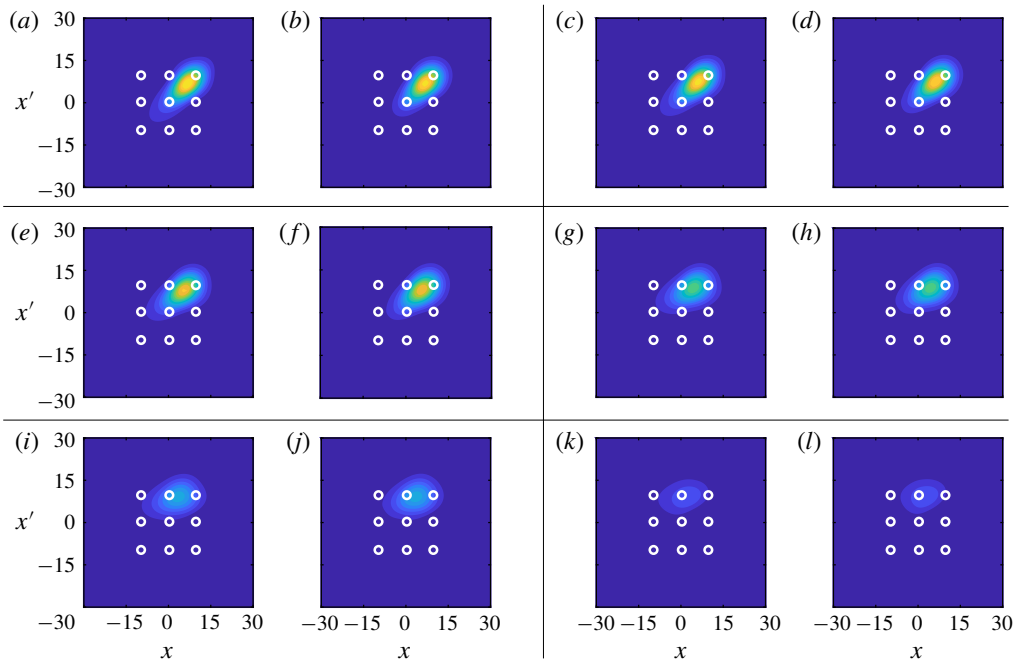

FIGURE 5. Cross-correlation as a function of x and x' for fixed time-lag values (a,b) $\tau = 0$; (c,d) $\tau = 1$; (e,f) $\tau = 2$; (g,h) $\tau = 4$; (i,j) $\tau = 6$; (k,l) $\tau = 10$. In each case, the left-hand plot shows the true correlations, and the right-hand plot shows the estimated values using three probes, which lead to known cross-correlations at the locations indicated by the small circles. The contour levels are the same in each panel and range from zero to the maximum values of the true correlation at $\tau = 0$.

In contrast, the new method is able to use this additional information to improve the estimate near the second probe without degrading the estimate near the original probe, leading to a small reduction in total error.

In the final case, the original probe at $x = 0$ is removed, leaving a single probe in the low-energy location $x = -10$. At this point, the underlying assumption of the rank-1 model – that the solution is dominated by the leading resolvent mode – is false. This is representative of the situation that will be encountered in real turbulent flows. Because of this, the rank-1 method leads to large over-predictions of the PSD and an error in excess of 1000 %. In contrast, the new method is able to use the information provided by this poorly placed probe to provide a reasonable estimate, albeit with higher error than is achieved using a well-placed probe. The moderate under-prediction of the PSD observed in this case can be attributed to neglecting the unobservable portions of $\boldsymbol{S}_{ff}$.

3.2. *Turbulent channel flow*

3.2.1. *Flow parameters, simulation and data processing*

Next, we apply the our resolvent-based estimation method to an incompressible turbulent channel flow at friction Reynolds number $Re_\tau = 187$, defined in terms of the friction velocity U_τ and the kinematic viscosity ν. Wall units, denoted by $+$ superscripts, are also defined in terms of U_τ and ν. This flow provides a convenient

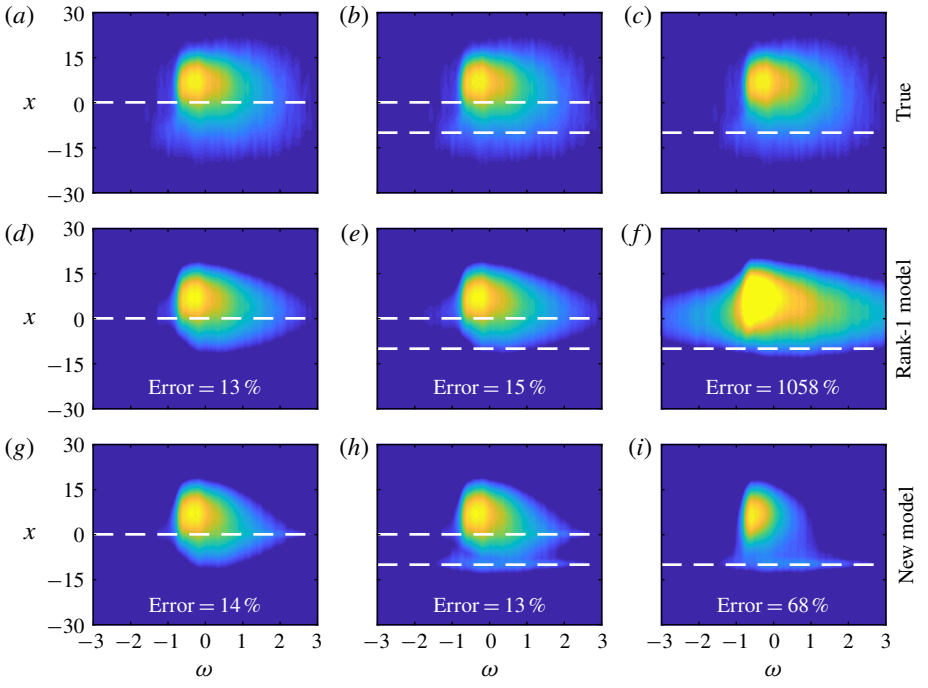

FIGURE 6. Power spectral density as a function of ω and x: (*a–c*) true values repeated for ease of comparison; (*d–f*) estimated values from the rank-1 model of Beneddine *et al.* (2016); (*g–i*) estimated values from the new model presented in this paper. The estimates are based on the following probe locations: (*a,d,g*) $x = 0$; (*b,e,h*) $x = -10$ and 0; (*c,f,i*) $x = -10$. The contour levels are the same as figure 1.

test case for application of the method to a real, nonlinear, turbulent flow. However, it is important to note that the results at this low Reynolds number may or may not extend to higher Reynolds numbers.

The flow is computed via direct numerical simulation (DNS) of the incompressible Navier–Stokes equations in a domain of size $L_x/h = 2\pi$, $L_y/h = 2$ and $L_z = \pi$, where x, y, and z are the streamwise, wall-normal and spanwise dimensions and h is the channel half-width. The flow is driven by imposing a constant mass flux in the streamwise direction and is integrated in the form of evolution equations for the wall-normal vorticity and for the Laplacian of the wall-normal velocity (Kim, Moin & Moser 1987). The periodic directions x and z are discretized using 64 Fourier modes in each direction with a 3/2 dealiasing rule, and the wall-normal direction y is discretized using 129 Chebyshev polynomials. The equations are advanced in time using a variable-time-step, third-order, semi-implicit Runge–Kutta integrator (Moser, Kim & Mansour 1999) with a Courant–Friedrichs–Lewy (CFL) number of 0.5, and the total simulation time is $tu_\tau/h \approx 80$. To facilitate post processing, the data are linearly interpolated in time to 10 000 evenly spaced time instances with $\Delta t^+ = 1.5$.

The simulation data are used to compute the cross-spectral density tensor $\boldsymbol{S_{qq}}$, where $\boldsymbol{q} = [u, v, w]^T$ and u, v, and w are the streamwise, wall-normal and spanwise velocities, respectively. Since the flow is periodic in x and z, the cross-spectral density is a function of wavenumber in these directions, i.e. $\boldsymbol{S_{qq}} = \boldsymbol{S_{qq}}(y, y'; k_x, k_z, \omega)$. The cross-spectral density is estimated using Welch's (1967) method. The flow data are divided

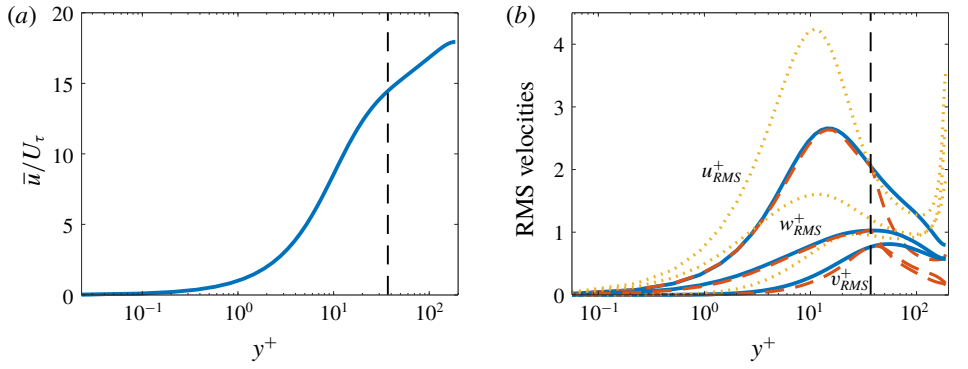

FIGURE 7. (*a*) Mean and (*b*) root-mean-squared velocities. Solid lines: true values calculated from the DNS data. Dashed lines: estimates obtained from the model using measurements at $y^+ = 37$ ($y/h = 0.2$). Dotted lines: estimates based on a white noise assumption. The input location is demarcated in the figure by the vertical dashed line.

into overlapping blocks each containing N_{fft} instantaneous snapshots of the flow. A discrete Fourier transform in x, z and t is applied to each block, leading to Fourier modes of the form $\hat{\boldsymbol{q}}_j(y; k_x, k_z, \omega)$ for $j = 1, 2, \ldots, N_b$, where N_b is the total number of blocks. Then, the cross-spectral density is estimated as

$$\boldsymbol{S}_{\boldsymbol{qq}}(y, y'; k_x, k_z, \omega) = \frac{1}{N_b} \sum_{j=1}^{N_b} \hat{\boldsymbol{q}}_j(y; k_x, k_z, \omega) \hat{\boldsymbol{q}}_j^*(y'; k_x, k_z, \omega). \tag{3.6}$$

Finally, the estimated cross-spectra are further averaged according to the symmetries described by Sirovich (1987), which ensures that the estimated cross-spectra are symmetric with respect to reflection across the channel centre line and to 180° rotation about the x-axis. We use blocks containing $N_{fft} = 256$ instantaneous snapshots with 75 % overlap, leading to $N_b = 156$ blocks, and a rectangular window function, which has the advantage of maintaining a discrete equivalence between quantities averaged over time or integrated over frequency. We have verified that our results are insensitive to these choices.

3.2.2. *Linearized Navier–Stokes equations*

The resolvent operators required for the model are obtained from the incompressible Navier–Stokes equations

$$\frac{\partial \boldsymbol{u}}{\partial t} + \bar{\boldsymbol{u}} \cdot \nabla \boldsymbol{u} + \boldsymbol{u} \cdot \nabla \bar{\boldsymbol{u}} + \nabla p - \frac{1}{Re_\tau} \nabla \cdot \left[\frac{\nu_T}{\nu} (\nabla \boldsymbol{u} + \nabla \boldsymbol{u}^{\mathrm{T}}) \right] = \boldsymbol{f}_{\boldsymbol{u}}, \tag{3.7a}$$

$$\nabla \cdot \boldsymbol{u} = 0, \tag{3.7b}$$

where $\boldsymbol{u} = [u, v, w]^{\mathrm{T}}$ is a vector of velocity disturbances, $\bar{\boldsymbol{u}} = [\bar{u}, 0, 0]$ is the mean velocity and p is the pressure disturbance. The mean streamwise velocity is computed from the DNS data and is shown in figure 7(*a*).

Following previous work (Reynolds & Hussain 1972; del Álamo & Jiménez 2006; Hwang & Cossu 2010; Moarref & Jovanović 2012; Illingworth, Monty & Marusic 2018), we have included an eddy viscosity model in the form of the total viscosity

function $\nu_T(y)$. These references and others have shown that including an eddy viscosity substantially improves the predictive capabilities of linearized models of the Navier–Stokes equations for wall-bounded flows, and recent work has shown similar benefits for free-shear flows (Pickering *et al.* 2019). Of particular relevance, Morra *et al.* (2019) recently showed that improved predictions of the statistics of a turbulent channel flow can be obtained by including an eddy viscosity for a resolvent model forced by white noise. By including an eddy viscosity in our method, we automatically inherit this improvement, while also using data to obtain an improved estimate of the forcing compared to a white noise assumption. Details of our eddy viscosity formulation are consistent with those of Illingworth *et al.* (2018) and can be found there.

Since the linearized equations are homogeneous in x and z, we can apply Fourier transforms in these directions and obtain an equation for each (k_x, k_z) wavenumber pair in the form of equation (2.7) with

$$\mathcal{A} = \mathrm{i}k_x A_x + A_y \frac{\partial}{\partial y} + \mathrm{i}k_z A_z - k_x^2 A_{xx} + A_{yy} \frac{\partial^2}{\partial y^2} - k_z^2 A_{zz}, \tag{3.8}$$

$\mathcal{G} = \mathrm{diag}([1,\ 1,\ 1,\ 0])$ and $\boldsymbol{q} = [u,\ v,\ w,\ p]^{\mathrm{T}}$. The matrices in (3.8) are provided in appendix B. The wall-normal direction y is discretized using 201 Chebyshev polynomials, and no-slip boundary conditions are applied at the walls.

We choose the known quantity $\boldsymbol{y}$ to be the three velocity components at $y/h = 0.2$, which in inner units corresponds to $y^+ = 37$. This is the same y/h value considered by Illingworth *et al.* (2018) in their recent Kalman filter study, although the y^+ value is different due to differing Reynolds numbers.

To visualize the results, we will focus on the velocity energy spectra, which are obtained from the cross-spectral density tensor as

$$\boldsymbol{E_{qq}}(y;\, k_x, k_z, \omega) = \boldsymbol{S_{qq}}(y, y;\, k_x, k_z, \omega). \tag{3.9}$$

3.2.3. *Root-mean-squared velocities*

We begin by examining the root-mean-squared (r.m.s.) velocity fluctuations, which are obtained by integrating $\boldsymbol{E_{qq}}(y;\, k_x, k_z, \omega)$ in k_x, k_z and ω and taking the square root. The true r.m.s. velocity fluctuations computed from the DNS data and those obtained from the model are compared in figure 7(*b*) as a function of y^+. The r.m.s. values are accurately estimated for all three velocity components in the near-wall region, specifically for $y^+ \lesssim 45$ ($y/h \lesssim 0.25$). The streamwise and spanwise velocity estimates are especially accurate, while slightly larger discrepancies are observed for the wall-normal velocity. Notably, the model accurately captures both the location and magnitude of the u_{rms} peak. For larger values of y^+, the r.m.s. values quickly fall below the DNS values. Results in the following section show that this under prediction is primarily due to missing energy at small scales, which do not have a footprint at the probe location. This missing energy could potentially be recovered by appropriate modelling of the $\boldsymbol{E}_{ij}$ terms that have been set to zero, as discussed in § 4.

We also show in this figure results obtained by assuming a spatially uncorrelated forcing of the form $\boldsymbol{S_{ff}} = p(\omega)\boldsymbol{I}$, as in Morra *et al.* (2019). This is similar to a classical white noise model (Farrell & Ioannou 1993; Jovanović & Bamieh 2001), except that the amplitude of the forcing at each frequency is determined by matching the PSD of the streamwise velocity. The estimated r.m.s. values are less accurate over most of the channel, and still worse results (not shown) are obtained using a true white noise

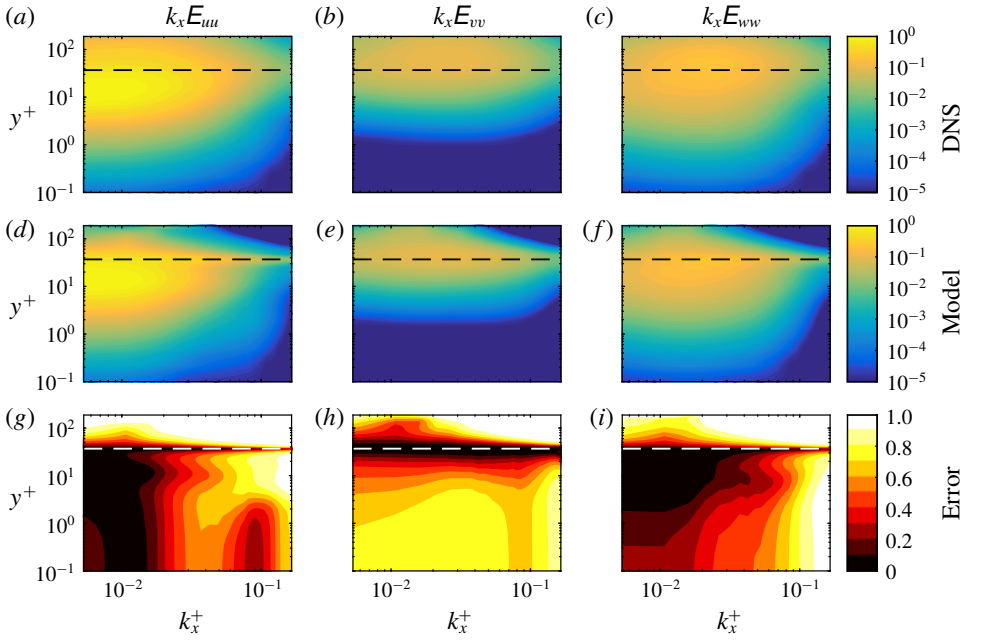

FIGURE 8. Premultiplied energy spectra as a function of streamwise wavenumber k_x^+ and wall-normal distance y^+. (*a–c*) DNS. (*d–f*) Estimates from the model. (*g–i*) Error metric defined by (3.10). Columns from left to right: streamwise velocity, wall-normal velocity, spanwise velocity. The horizontal dashed lines show the location of the known input data, $y^+ = 37$.

assumption ($p(\omega) = p_0$). These results demonstrate that the resolvent-based estimation method leads to an improved estimate of the nonlinear forcing and resulting flow statistics compared to models based on assumptions of white noise and spatially uncorrelated forcing. Accordingly, we do not further consider these model in what follows and focus solely on results from our resolvent-based estimation method.

3.2.4. *Energy spectra*

Figures 8–10 show the energy spectrum for each velocity component as a function of y^+ and k_x^+, k_z^+, and ω^+, respectively. In each case, the energy has been integrated over the other two Fourier variables. The energies have been premultiplied by the appropriate wavenumber or frequency to account for the logarithmic axes in wave space. The contour levels are logarithmically spaced and span five orders of magnitude, with the highest level equal to the maximum value of the DNS streamwise velocity spectrum. The same levels are used in all subplots so that magnitudes can be directly compared. The true spectra computed from the DNS data appear in the top row of each figure, and the corresponding model estimates appear in the second row. The error of the estimate is quantified by the metric

$$\frac{|\tilde{\boldsymbol{E}}_{qq} - \boldsymbol{E}_{qq}|}{\boldsymbol{E}_{qq}}, \tag{3.10}$$

which is shown in the third row of each figure.

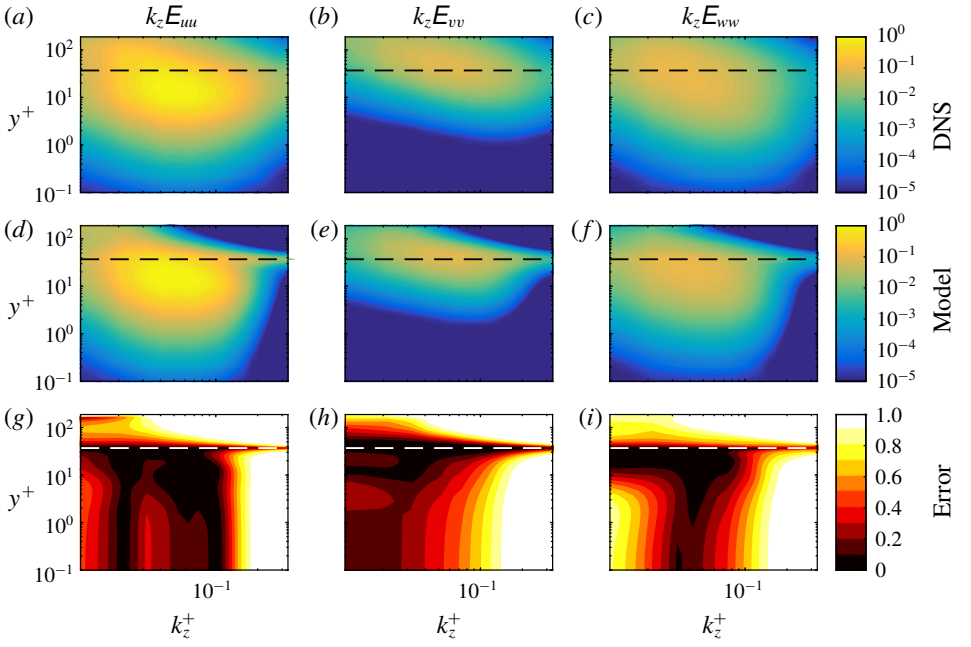

FIGURE 9. Premultiplied energy spectra as a function of spanwise wavenumber k_z^+ and wall-normal distance y^+. Details are the same as figure 8.

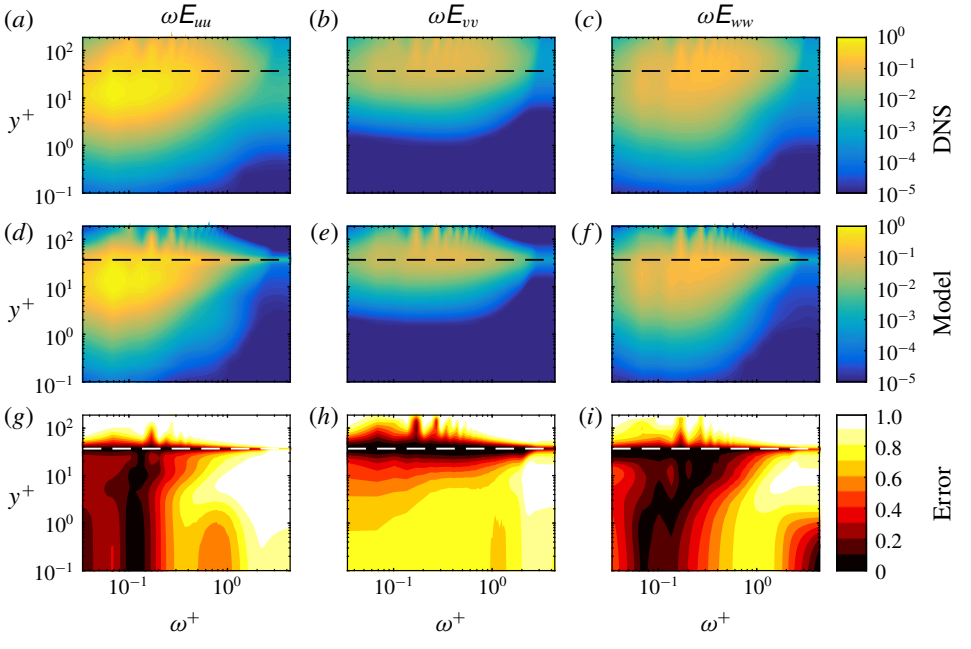

FIGURE 10. Premultiplied energy spectra as a function of frequency ω^+ and wall-normal distance y^+. Details are the same as figure 8.

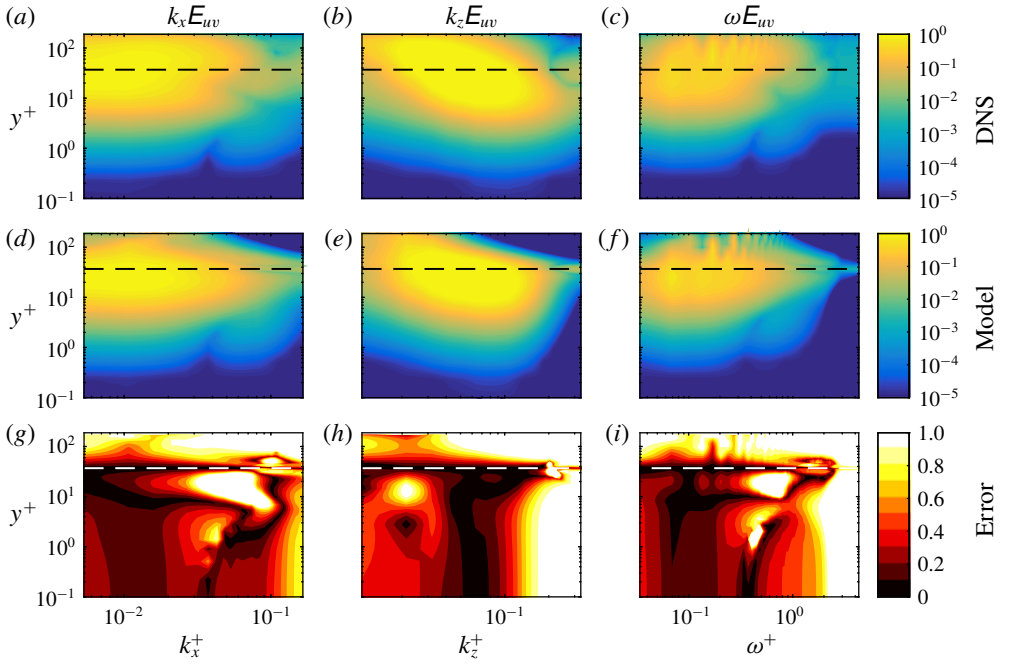

FIGURE 11. Premultiplied energy spectra of the uv Reynolds stresses. (*a–c*) DNS. (*d–f*) Estimates from the model. (*g–i*) Error metric defined in (3.10). Columns from left to right: k_x wavenumber spectra, k_z wavenumber spectra, frequency spectra. The horizontal dashed lines show the location of the known input data, $y^+ = 37$.

In all cases, the model captures the energy distribution of all three velocity components with reasonable accuracy for $y^+ \lesssim 45$, except at the highest wavenumbers and frequencies. As was the case for the r.m.s., the wall-normal velocity is the least accurately predicted. The amplitudes and locations of the energy peaks in $(y^+, k_x^+, k_z^+, \omega^+)$ space are well captured by the model. On the other hand, the model under-predicts the energy at all wavenumbers and frequencies for higher values of y^+. The highest wavenumbers and frequencies are correctly predicted only near the position of the known input data at $y^+ = 37$ (horizontal dashed lines in the figures). This observation can be explained by the smaller wall-normal footprint of smaller scale motions. A small scale eddy detected by the probe will impact the flow only close to the probe location. Similarly, a small scale eddy away from the probe location will not be detected at all. As a result, small scales can only be detected near the probe, leading to accurate predictions near the probe, but significant under predictions of small scale energy away from the probe.

The resolvent-based estimation method also provides estimates of cross-power-spectral densities such as the uv Reynolds stress E_{uv}, which is shown as a function of k_x, k_z, and ω in figure 11. Again, accurate results are obtained for low and moderate wavenumbers and frequencies, with a significant under prediction for smaller scales except near the probe.

The ability of the resolvent-based estimation method to capture various scales can be further assessed by examining the power spectra as a function of both streamwise and spanwise length scales. Figure 12 shows power spectra as a function of the wavelengths λ_x^+ and λ_z^+ at the fixed wall-normal position $y^+ = 9$. These wavelengths

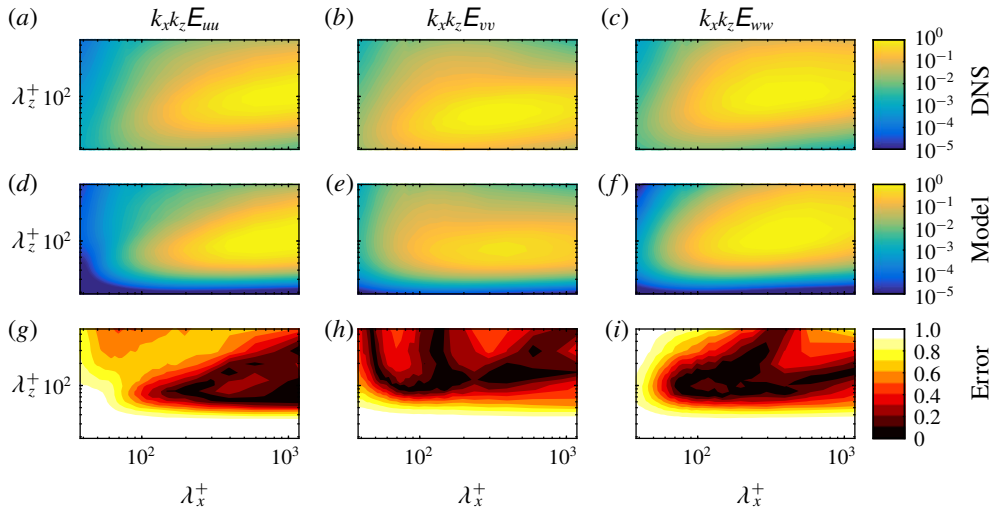

FIGURE 12. Premultiplied energy spectra as a function of streamwise wavelength λ_x^+ and spanwise wavelength λ_z^+. (*a–c*) DNS. (*d–f*) Estimates from the model. (*g–i*) Error as defined by (3.10). Columns from left to right: streamwise velocity, wall-normal velocity, spanwise velocity.

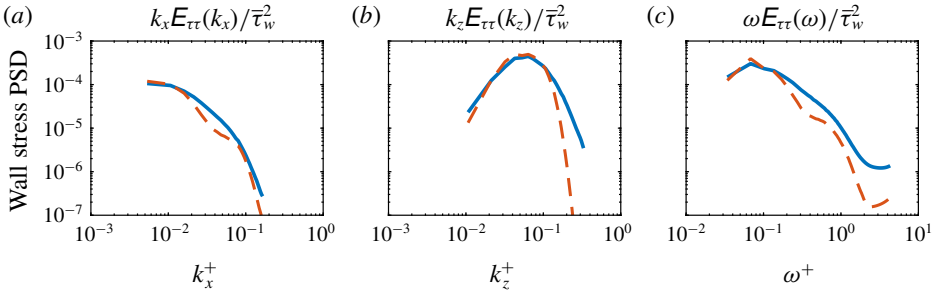

FIGURE 13. Premultiplied energy spectra of wall shear stress stresses. Solid lines: DNS. Dashed lines: estimates from the model. Columns from left to right: k_x wavenumber spectra, k_z wavenumber spectra, frequency spectra.

are related to the previous considered wavenumbers as $\lambda_{x,z}^+ = 2\pi/k_{x,z}^+$. The estimates are accurate for large scales as seen previously, with especially low errors near the energy peak for each velocity component. McKeon & Sharma (2010) showed that these high-energy wavelength pairs are well approximated by the leading few modes of the resolvent operator, which partially explains the success of the resolvent-based estimated method there. Figure 12 also highlights that the energy is most severely under predicted for small spanwise length scales. These results also reinforce the observation from previous works (Encinar *et al.* 2018) that detached fluid motions far from the wall are not correctly captured by linear models, probably because their limited wall-normal extent does not allow for their full reconstruction.

One key quantity for which estimates may be of interest is the wall shear stress, especially for future developments in the context of wall-modelled large-eddy simulation. Figure 13 shows premultiplied spectra of the streamwise wall shear stress as a function of k_x^+, k_z^+, and ω^+. The estimates are accurate for low and

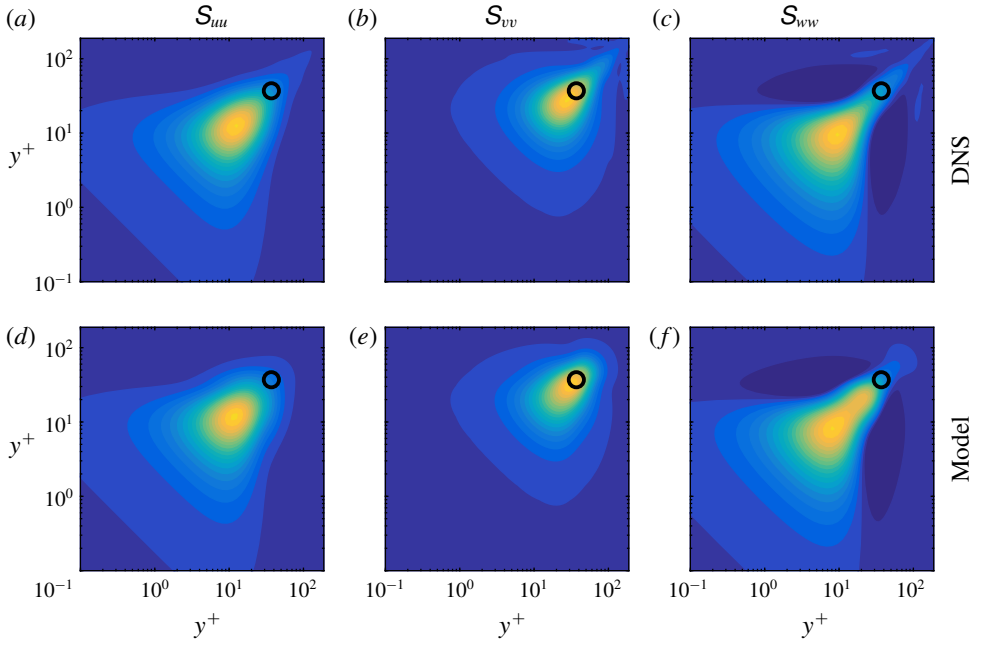

FIGURE 14. Cross-spectral density for the spectral parameters $\lambda_x^+ \approx 700$, $\lambda_z^+ \approx 100$ and $c_p \approx 10$. (*a–c*) DNS. (*d–f*) Estimates obtained from the model. Columns from left to right: streamwise, wall-normal and spanwise velocity, respectively. The black circle shows the input location where the DNS data are provided to the model.

moderate wavenumbers and frequency, with the largest errors observed for high spanwise wavenumbers. The error of the total (integrated) wall shear stress power is 8 %.

3.2.5. *Cross-spectra*

In addition to the energy spectra considered so far, the model also provides predictions for cross-spectra. An example is shown in figure 14. The CSD is plotted as a function of y^+ and $(y^+)'$ for the streamwise and spanwise wavenumbers $\lambda_x^+ = 700$ and $\lambda_z^+ = 100$, respectively, and the phase speed $c_p = 10$, which are typical values at which coherent structures are expected to appear (Sharma & McKeon 2013). The model uses the input data indicated by the black circles, and accurately reproduces the CSD for all three velocity components. Since coherent structures are closely related to the CSD tensor (Towne *et al.* 2018), the accuracy of the CSD estimates suggests that the influence of the dominant coherent structures has been captured by the resolvent-based estimation method.

3.2.6. *Autocorrelations and convection velocity*

Next, we consider the space–time correlations

$$\boldsymbol{C}_{\boldsymbol{qq}}(y, y', \delta x, \delta z, \delta t) = E\{\boldsymbol{q}(x, y, z, t)\boldsymbol{q}^*(x + \delta x, y', z + \delta z, t + \delta t)\}, \tag{3.11}$$

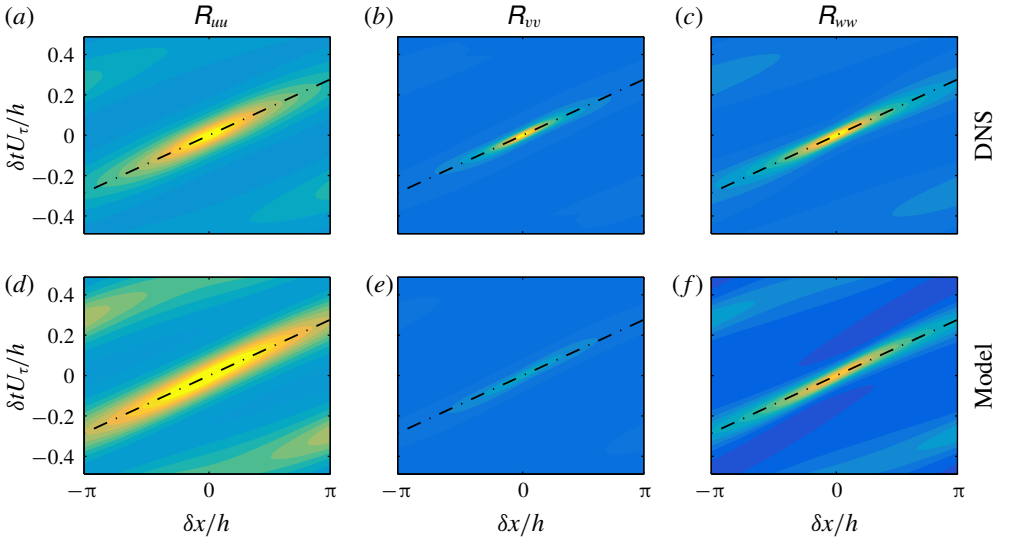

FIGURE 15. Autocorrelation as a function of streamwise separation δx and temporal separation δt at $y^+ = 9$ ($y/h = 0.05$). (*a–c*) DNS. (*d–f*) Estimates obtained from the model. Columns from left to right: streamwise, wall-normal and spanwise velocity, respectively. The contour levels are linearly spaced between 90 % and −20 % of the maximum value of the DNS autocorrelation of each velocity component. The slope of the dashed lines gives the inverse of the dominant convection velocity.

where the expectation is taken over all x, z and t. These correlations can be recovered from the cross-spectra discussed so far by taking inverse Fourier transforms,

$$\boldsymbol{C_{qq}}(y, y', \delta x, \delta z, \delta t) = \frac{1}{(2\pi)^3} \int_{-\infty}^{\infty}\int_{-\infty}^{\infty}\int_{-\infty}^{\infty} \boldsymbol{S_{qq}}(y, y', k_x, k_z, \omega) \mathrm{e}^{\mathrm{i}k_x\delta x} \mathrm{e}^{\mathrm{i}k_z\delta z} \mathrm{e}^{\mathrm{i}\omega\delta t}\, \mathrm{d}k_x\, \mathrm{d}k_z\, \mathrm{d}\omega. \tag{3.12}$$

We will focus on the autocorrelations

$$\boldsymbol{R_{qq}}(y; \delta x, \delta z, \delta t) = \boldsymbol{C_{qq}}(y, y, \delta x, \delta z, \delta t). \tag{3.13}$$

As an example, we examine the autocorrelations as a function of the streamwise and temporal lag variables δx and δt, respectively, at a fixed wall-normal location $y/h = 0.05$ ($y^+ = 9$). Figure 15 shows the autocorrelation of each velocity component as a function of δx and δt, i.e. the space–time autocorrelations along the streamwise direction. The contour levels are logarithmically spaced between the maximum value of the streamwise autocorrelation from DNS and span five orders of magnitude. The same levels are used in all subplots. The inverse slope of the band of high correlation in each plot provides a measure of the convection velocity of disturbances. At this wall-normal location, the convection velocity is approximately $11U_\tau$ and is accurately approximated by the estimate for all three velocity components. The correlation magnitudes are also well approximated aside from a moderate under prediction of the peak wall-normal velocity correlations.

Figure 16 shows the convection velocity calculated from the DNS data and resolvent-based estimates as a function of wall-normal position. Following previous

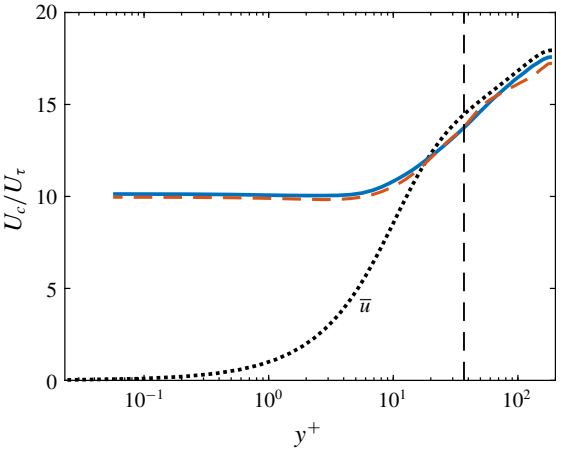

FIGURE 16. Convection velocity as a function of y^+. Solid lines: true values calculated from the DNS data. Dashed lines: estimates obtained from the model using measurements at $y^+ = 37$ $(y/h = 0.2)$. This input location is demarcated in the figure by the vertical dashed line, and the mean velocity profile is shown as a dotted line for reference.

authors (Choi & Moin 1990; Park & Moin 2016), the convection velocity is defined as

$$U_c(y) = \arg\max_U \int_{-\infty}^{\infty} R_{uu}(y, Ut, 0, t)\,\mathrm{d}t, \tag{3.14}$$

i.e. the direction in x–t space along which the integrated streamwise velocity correlation is maximum.

Consistent with the observation of Kim & Hussain (1993) and del Álamo & Jiménez (2009), the convection velocity computed from the DNS data is approximately equal to the mean streamwise velocity for $y^+ \gtrsim 10$ and asymptotes to a constant value of about $10U_\tau$ near the wall. These trends are accurately captured by convection velocities computed from the estimated autocorrelations. The near-wall asymptotic convection velocity is under predicted by just 1.7 %, and the error in the outer region is less than the difference between the true convection velocity and the mean velocity up to $y^+ \approx 100$.

4. Conclusions

Building on the work of Beneddine *et al.* (2016), Gómez *et al.* (2016*a*) and Zare *et al.* (2017), this paper introduces a method for estimating space–time flow statistics from a limited set of known values. The method is based on the resolvent methodology developed by McKeon & Sharma (2010) and the statistical interpretation of this theory proposed by Towne *et al.* (2018). The central idea of our approach is to (partially) infer the nonlinear term of the linearized Navier–Stokes equations using limited flow data. This nonlinear term is then used as a forcing acting on the resolvent operator to reconstruct unknown statistics of the flow.

The resolvent-based estimation method was demonstrated using two example problems. First, it was applied to the complex Ginzburg–Landau equation, which serves as a convenient model of a convectively unstable flow. Using input data from three probe locations, the method provided good estimates of the unknown power

spectra, cross-spectra and space–time correlations within the energetic regions of ω-x or τ-x space. Comparisons were then made with the rank-1 model proposed by Beneddine *et al.* (2016). The two methods gave similar results when the probes were placed at locations dominated by a single resolvent mode, but the new method gave superior results when the probes were placed at locations that violate this underlying assumption of the rank-1 model. The improved behaviour in this case is important for turbulent flows, which cannot in general be described by a single resolvent mode. Furthermore, the estimates provided by the new method improve with the addition of more known input data and converge in the limit of complete knowledge of the flow, unlike the rank-1 method.

Second, we applied our method to a turbulent channel at friction Reynolds number $Re_\tau = 187$. Using data exclusively from the wall-normal location $y/h = 0.2$ ($y^+ = 37$), the method provides good estimates of the velocity energy spectra and autocorrelations for $y \lesssim 0.25$ ($y^+ \lesssim 45$). The energies and autocorrelations are under-predicted further away from the wall due to missing energy at small scales that requires additional modelling to capture. If the success of the model in the near-wall region using knowledge of the interior flow persists at higher Reynolds numbers, it could be useful for designing new wall models for large-eddy simulation that are capable of capturing fluctuations of wall quantities such as shear stress and heat transfer and near-wall velocities that play an important role, for example, in particle laden flows. More broadly, the method could be useful for flow estimation and control – the statistical estimates obtained by our method can be used to obtain real-time flow estimates using approaches such as linear stochastic estimation (Adrian 1994; Bonnet *et al.* 1994) and H_1 and H_2 frequency response functions (Bendat & Piersol 1990; Sasaki *et al.* 2017).

Additional work is required to understand the channel flow observations, further assess the impact of the location of the known input data, and determine whether the results described in this paper will extend to higher Reynolds numbers and other types of turbulent flows. The properties and performance of the method should also be directly compared to other approaches that use the linearized flow equations as the basis for flow estimation, including the recent Kalman-filter-based approach described by Illingworth *et al.* (2018).

The method itself could also be further improved by modelling the portions of the forcing cross-spectral density that cannot be observed using the known data. In the current formulation, these terms are simply set to zero, and there exist several possible alternatives. One is to assume that the unobserved forcing is uncorrelated with the observed part and with itself, leading to the approximation

$$\boldsymbol{S}_{ff} = [\boldsymbol{V}_1 \;\; \boldsymbol{V}_2] \begin{bmatrix} \boldsymbol{F}_{11} & \boldsymbol{0} \\ \boldsymbol{0} & a\boldsymbol{I} \end{bmatrix} [\boldsymbol{V}_1 \;\; \boldsymbol{V}_2]^*. \tag{4.1}$$

An appropriate value for the scalar amplitude a could be determined from the amplitudes of the known $\boldsymbol{F}_{11}$ terms.

Another possibility is to choose the unobservable terms by insisting that the estimated $\boldsymbol{S}_{ff}$ projects exclusively onto the first n singular modes of $\mathcal{R}_q$, where n is the number of measurements. In other words, the forcing would be made unique by limiting its influence to the leading modes of $\mathcal{R}_q$. This possibility is similar to a suggestion made by Beneddine *et al.* (2017), except here the expansion coefficients are treated as statistical quantities rather than complex scalars. As shown by Towne *et al.* (2018), this statistical treatment removes a fundamental accuracy restriction

imposed by treating the expansion coefficients as deterministic scalars and allows for a convergent approximation. While neither of these aforementioned modifications are likely optimal, they highlight the potential for further improvements within the framework of our resolvent-based estimation method.

Acknowledgements

A.T. thanks E. Martini, A. Cavalieri and P. Jordan for fruitful discussion that helped improve this work. A.L.-D. was partially supported by NASA under grant NNX15AU93A and by ONR under grant N00014-16-S-BA10.

Appendix A. Least-squares approximation of forcing

Let us compute the approximation of $\boldsymbol{S}_{ff}$ obtained using the pseudo-inverse of $\mathcal{R}_y$, which can be written in terms of the SVD (2.13) as

$$\mathcal{R}_y^+ = \boldsymbol{V}_y \boldsymbol{\Sigma}_y^+ \boldsymbol{U}_y^*, \tag{A 1}$$

where $\boldsymbol{\Sigma}_y^+ = [\boldsymbol{\Sigma}_1^{-1}\ \boldsymbol{0}]^{\mathrm{T}}$. Applying the pseudo-inverse and its complex conjugate to the left- and right-hand sides of (2.12*a*), respectively, gives the pseudo-inverse approximation of $\boldsymbol{S}_{ff}$,

$$\begin{aligned}
\boldsymbol{S}_{ff}^{LS} &= \mathcal{R}_y^+ \boldsymbol{S}_{yy} (\mathcal{R}_y^+)^* && \text{(A 2}a\text{)}\\
&= \boldsymbol{V}_y \boldsymbol{\Sigma}_y^{-1} \boldsymbol{U}_y^* \boldsymbol{S}_{yy} \boldsymbol{U}_y \boldsymbol{\Sigma}_y^{-1} \boldsymbol{V}_y^* && \text{(A 2}b\text{)}\\
&= [\boldsymbol{V}_1\ \boldsymbol{V}_2] \begin{bmatrix} \boldsymbol{\Sigma}_1^{-1} & \boldsymbol{0} \end{bmatrix}^T \boldsymbol{U}_y^* \boldsymbol{S}_{yy} \boldsymbol{U}_y \begin{bmatrix} \boldsymbol{\Sigma}_1^{-1} & \boldsymbol{0} \end{bmatrix} [\boldsymbol{V}_1\ \boldsymbol{V}_2]^* && \text{(A 2}c\text{)}\\
&= \boldsymbol{V}_1 \boldsymbol{\Sigma}_1^{-1} \boldsymbol{U}_y^* \boldsymbol{S}_{yy} \boldsymbol{U}_y \boldsymbol{\Sigma}_1^{-1} \boldsymbol{V}_1^* && \text{(A 2}d\text{)}\\
&= \boldsymbol{V}_1 \boldsymbol{F}_{11} \boldsymbol{V}_1^*, && \text{(A 2}e\text{)}
\end{aligned}$$

with $\boldsymbol{F}_{11}$ given by (2.16). Equation (A 2*e*) is identical to (2.17), which shows that setting the unknown $\boldsymbol{F}_{ij}$ terms to zero is equivalent to a least-squares, pseudo-inverse approximation of $\boldsymbol{S}_{ff}$.

Appendix B. Linearized incompressible Navier–Stokes operators

The matrices defining the linearized incompressible Navier–Stokes equations in (2.7) and (3.8) are,

$$\boldsymbol{A}_x = \begin{bmatrix} \bar{u} & -\nu_T' & 0 & 1 \\ 0 & \bar{u} & 0 & 0 \\ 0 & 0 & \bar{u} & 0 \\ 1 & 0 & 0 & \bar{u} \end{bmatrix}, \quad \boldsymbol{A}_y = \begin{bmatrix} -\nu_T' & 0 & 0 & 0 \\ 0 & -2\nu_T' & 0 & 1 \\ 0 & 0 & -\nu_T' & 0 \\ 0 & 1 & 0 & 0 \end{bmatrix}, \quad \boldsymbol{A}_z = \begin{bmatrix} 0 & 0 & 0 & 0 \\ 0 & 0 & 0 & 0 \\ 0 & -\nu_T' & 0 & 1 \\ 0 & 0 & 1 & 0 \end{bmatrix}, \tag{B 1}a\text{–}c$$

$$\boldsymbol{A}_0 = \begin{bmatrix} 0 & \dfrac{\partial \bar{u}}{\partial y} & 0 & 0 \\ 0 & 0 & 0 & 0 \\ 0 & 0 & 0 & 0 \\ 0 & 0 & 0 & 0 \end{bmatrix}, \quad \mathcal{G} = \begin{bmatrix} 1 & 0 & 0 & 0 \\ 0 & 1 & 0 & 0 \\ 0 & 0 & 1 & 0 \\ 0 & 0 & 0 & 0 \end{bmatrix}, \quad \boldsymbol{B} = \begin{bmatrix} 1 & 0 & 0 \\ 0 & 1 & 0 \\ 0 & 0 & 1 \\ 0 & 0 & 0 \end{bmatrix}, \tag{B 2}a\text{–}c$$

and $\boldsymbol{A}_{xx} = \boldsymbol{A}_{yy} = \boldsymbol{A}_{zz} = -(1/Re_\tau)(\nu_T/\nu)\mathcal{G}$. We have defined $\nu_T' = (1/Re_\tau)(1/\nu)(\partial \nu_T/\partial y)$.

REFERENCES

ADRIAN, R. J. 1994 Stochastic estimation of conditional structure: a review. *Appl. Sci. Res.* **53** (3), 291–303.

DEL ÁLAMO, J. C. & JIMÉNEZ, J. 2006 Linear energy amplification in turbulent channels. *J. Fluid Mech.* **559**, 205–213.

DEL ÁLAMO, J. C. & JIMÉNEZ, J. 2009 Estimation of turbulent convection velocities and corrections to Taylor's approximation. *J. Fluid Mech.* **640**, 5–26.

BAGHERI, S., HENNINGSON, D. S., HOEPFFNER, J. & SCHMID, P. J. 2009 Input-output analysis and control design applied to a linear model of spatially developing flows. *Appl. Mech. Rev.* **62** (2), 020803.

BENDAT, J. S. & PIERSOL, A. G. 1990 *Random Data: Analysis and Measurement Procedures*. Wiley.

BENEDDINE, S., SIPP, D., ARNAULT, A., DANDOIS, J. & LESSHAFFT, L. 2016 Conditions for validity of mean flow stability analysis. *J. Fluid Mech.* **798**, 485–504.

BENEDDINE, S., YEGAVIAN, R., SIPP, D. & LECLAIRE, B. 2017 Unsteady flow dynamics reconstruction from mean flow and point sensors: an experimental study. *J. Fluid Mech.* **824**, 174–201.

BONNET, J. P., COLE, D. R., DELVILLE, J., GLAUSER, M. N. & UKEILEY, L. S. 1994 Stochastic estimation and proper orthogonal decomposition: complementary techniques for identifying structure. *Exp. Fluids* **17** (5), 307–314.

CHEN, K. K. & ROWLEY, C. W. 2011 H_2 optimal actuator and sensor placement in the linearised complex Ginzburg–Landau system. *J. Fluid Mech.* **681**, 241–260.

CHOI, H. & MOIN, P. 1990 On the space-time characteristics of wall-pressure fluctuations. *Phys. Fluids* **2** (8), 1450–1460.

ENCINAR, A., LOZANO-DURÉN, A. & JIMÉNEZ, J. 2018 Reconstructing channel turbulence from wall observations. In *Proceedings of the Summer Program*. Center for Turbulence Research, Stanford University.

FARRELL, B. F. & IOANNOU, P. J. 1993 Stochastic forcing of the linearized Navier–Stokes equations. *Phys. Fluids* **5** (11), 2600–2609.

GÓMEZ, F., BLACKBURN, H. M., RUDMAN, M., SHARMA, A. S. & MCKEON, B. J. 2016*a* A reduced-order model of three-dimensional unsteady flow in a cavity based on the resolvent operator. *J. Fluid Mech.* **798**, R2.

GÓMEZ, F., SHARMA, A. S. & BLACKBURN, H. M. 2016*b* Estimation of unsteady aerodynamic forces using pointwise velocity data. *J. Fluid Mech.* **804**, R4.

HUNT, R. E. & CRIGHTON, D. G. 1991 Instability of flows in spatially developing media. *Proc. R. Soc. Lond.* A **435**, 109–128.

HWANG, Y. & COSSU, C. 2010 Linear non-normal energy amplification of harmonic and stochastic forcing in the turbulent channel flow. *J. Fluid Mech.* **664**, 51–73.

ILLINGWORTH, S. J., MONTY, J. P. & MARUSIC, I. 2018 Estimating large-scale structures in wall turbulence using linear models. *J. Fluid Mech.* **842**, 146–162.

JEUN, J., NICHOLS, J. W. & JOVANOVIĆ, M. R. 2016 Input-output analysis of high-speed axisymmetric isothermal jet noise. *Phys. Fluids* **28** (4), 047101.

JOVANOVIĆ, M. & BAMIEH, B. 2001 Modeling flow statistics using the linearized Navier–Stokes equations. In *Proceedings of the 40th IEEE Conference on Decision and Control*, vol. 5, pp. 4944–4949. IEEE.

JOVANOVIĆ, M. R. & BAMIEH, B. 2005 Componentwise energy amplification in channel flows. *J. Fluid Mech.* **534**, 145–183.

KIM, J. & HUSSAIN, F. 1993 Propagation velocity of perturbations in turbulent channel flow. *Phys. Fluids* **5** (3), 695–706.

KIM, J., MOIN, P. & MOSER, R. 1987 Turbulence statistics in fully developed channel flow at low Reynolds number. *J. Fluid Mech.* **177**, 133–166.

MCKEON, B. J. & SHARMA, A. S. 2010 A critical-layer framework for turbulent pipe flow. *J. Fluid Mech.* **658**, 336–382.

MESEGUER, Á. & TREFETHEN, L. N. 2003 Linearized pipe flow to Reynolds number 107. *J. Comput. Phys.* **186** (1), 178–197.

MOARREF, R. & JOVANOVIĆ, M. R. 2012 Model-based design of transverse wall oscillations for turbulent drag reduction. *J. Fluid Mech.* **707**, 205–240.

MOARREF, R., JOVANOVIĆ, M. R., TROPP, J. A., SHARMA, A. S. & MCKEON, B. J. 2014 A low-order decomposition of turbulent channel flow via resolvent analysis and convex optimization. *Phys. Fluids* **26** (5), 051701.

MORRA, P., SEMERARO, O., HENNINGSON, D. S. & COSSU, C. 2019 On the relevance of Reynolds stresses in resolvent analyses of turbulent wall-bounded flows. *J. Fluid Mech.* **867**, 969–984.

MOSER, R. D., KIM, J. & MANSOUR, N. N. 1999 Direct numerical simulation of turbulent channel flow up to $Re_\tau = 590$. *Phys. Fluids* **11** (4), 943–945.

PARK, G. I. & MOIN, P. 2016 Space-time characteristics of wall-pressure and wall shear-stress fluctuations in wall-modeled large eddy simulation. *Phys. Rev. Fluids* **1** (2), 024404.

PICKERING, E. M., RIGAS, G., SIPP, D., SCHMIDT, O. T. & COLONIUS, T. 2019 Eddy viscosity for resolvent-based jet noise models. *AIAA Paper* no. 2019-2454.

REYNOLDS, W. C. & HUSSAIN, A. K. M. F. 1972 The mechanics of an organized wave in turbulent shear flow. Part 3. Theoretical models and comparisons with experiments. *J. Fluid Mech.* **54** (2), 263–288.

SASAKI, K., PIANTANIDA, S., CAVALIERI, A. V. G. & JORDAN, P. 2017 Real-time modelling of wavepackets in turbulent jets. *J. Fluid Mech.* **821**, 458–481.

SCHMID, P. J. 2007 Nonmodal stability theory. *Annu. Rev. Fluid Mech.* **39**, 129–162.

SCHMIDT, O. T., TOWNE, A., RIGAS, G., COLONIUS, T. & BRÈS, G. A. 2018 Spectral analysis of jet turbulence. *J. Fluid Mech.* **855**, 953–982.

SEMERARO, O., JAUNET, V., JORDAN, P., CAVALIERI, A. V. G. & LESSHAFFT, L. 2016 Stochastic and harmonic optimal forcing in subsonic jets. *AIAA Paper* no. 2016-2935.

SHAMPINE, L. F. & REICHELT, M. W. 1997 The Matlab ODE suite. *SIAM J. Sci. Comput.* **18** (1), 1–22.

SHARMA, A. S. & MCKEON, B. J. 2013 On coherent structure in wall turbulence. *J. Fluid Mech.* **728**, 196–238.

SIROVICH, L. 1987 Turbulence and the dynamics of coherent structures. ii. symmetries and transformations. *Q. Appl. Maths* **45** (3), 573–582.

SYMON, S., SIPP, D. & MCKEON, B. J. 2019 A tale of two airfoils: resolvent-based modelling of an oscillator versus an amplifier from an experimental mean. *J. Fluid Mech.* **881**, 51–83.

THOMAREIS, N. & PAPADAKIS, G. 2018 Resolvent analysis of separated and attached flows around an airfoil at transitional Reynolds number. *Phys. Rev. Fluids* **3**, 073901.

TOWNE, A., BRÈS, G. A. & LELE, S. K. 2016 Toward a resolvent-based statisitical jet-noise model. In *Annual Research Briefs*. Center for Turbulence Research, Stanford University.

TOWNE, A., BRÈS, G. A. & LELE, S. K. 2017 A statistical jet-noise model based on the resolvent framework. *AIAA Paper* no. 2017-3406.

TOWNE, A., SCHMIDT, O. T. & COLONIUS, T. 2018 Spectral proper orthogonal decomposition and its relationship to dynamic mode decomposition and resolvent analysis. *J. Fluid Mech.* **847**, 821–867.

WELCH, P. 1967 The use of fast Fourier transform for the estimation of power spectra: a method based on time averaging over short, modified periodograms. *IEEE Trans. Audio Electroacoust.* **15** (2), 70–73.

YEH, C.-A. & TAIRA, K. 2019 Resolvent-analysis-based design of airfoil separation control. *J. Fluid Mech.* **867**, 572–610.

ZARE, A., CHEN, Y., JOVANOVIĆ, M. R. & GEORGIOU, T. T. 2017 Low-complexity modeling of partially available second-order statistics: theory and an efficient matrix completion algorithm. *IEEE Trans. Autom. Control* **62** (3), 1368–1383.

ZARE, A., JOVANOVIĆ, M. R. & GEORGIOU, T. T. 2017 Colour of turbulence. *J. Fluid Mech.* **812**, 636–680.